The Imaging Photopolarimeter Experiment on Pioneer 11

Abstract. *For 2 weeks continuous imaging, photometry, and polarimetry observations were made of Jupiter and the Galilean satellites in red and blue light from Pioneer 11. Measurements of Jupiter's north and south polar regions were possible because the spacecraft trajectory was highly inclined to the planet's equatorial plane. One of the highest resolution images obtained is presented here along with a comparison of a sample of our photometric and polarimetric data with a simple model. The data seem consistent with increased molecular scattering at high latitudes.*

The imaging photopolarimeter is a pointable telescope with an aperture of 2.5 cm that utilizes the spin motion of the spacecraft to scan across the object. It may be stepped in a direction perpendicular to that of the spacecraft spin, thus forming a two-dimensional map. The specifications of the instrument were published for Pioneer 10 (*1*) and are essentially the same for Pioneer 11. A detailed description of the polarimeter is given in (*2*). The instrument provides observations for several studies with the use of three different diaphragms in the focal plane. Some of the results obtained with Pioneer 10 have been published: the largest diaphragm, 2.3° by 2.3°, has been used for studies of background starlight (*3*) and of the zodiacal light and the asteroid belt (*4*); the 0.5° by 0.5° diaphragm was used for photometry and polarimetry of Jupiter (*5*); the smallest diaphragm, 0.3° by 0.3°, has been used for photometry (*6*), for imaging (*7, 8*), for the study of cloud forms (*9*), and for astrometry (*10*).

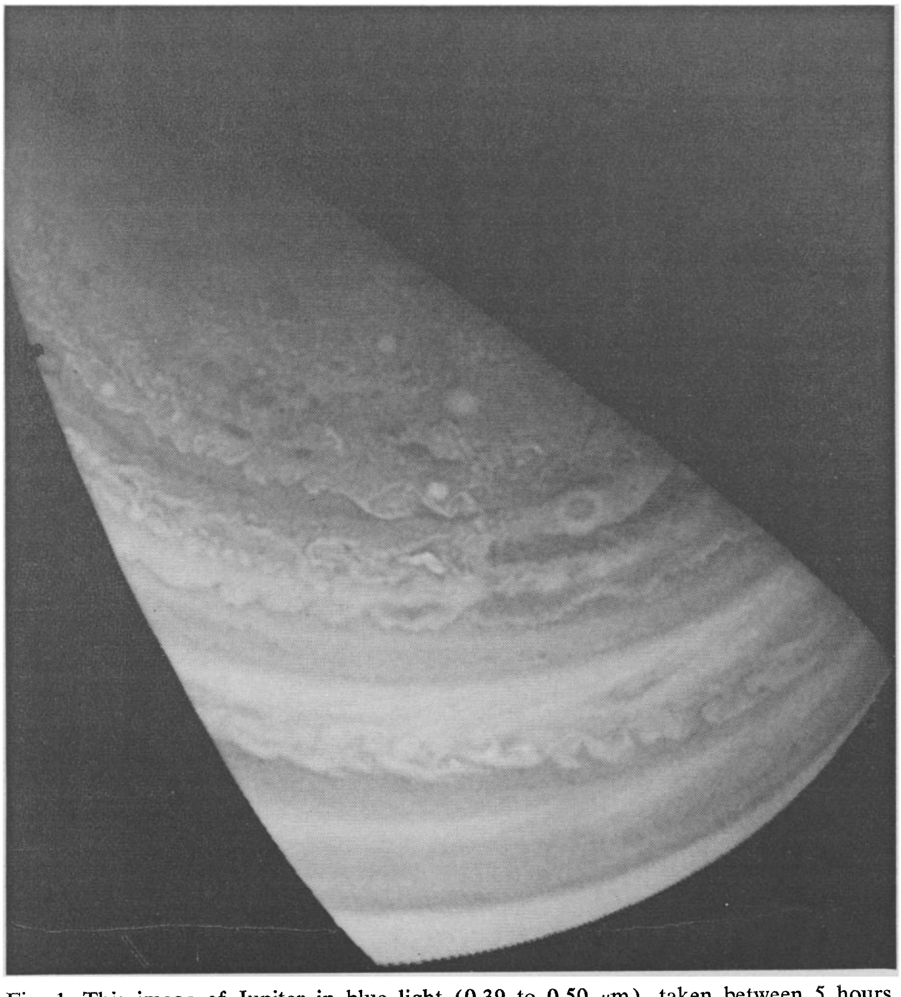

Fig. 1. This image of Jupiter in blue light (0.39 to 0.50 μm), taken between 5 hours, 52 minutes and 6 hours, 58 minutes after pericenter, shows a segment of the planet centered in the northern hemisphere. At the midtime of the image the latitude of the subspacecraft point was +49°, and its system II longitude was 3°. Latitudes up to 73° are seen. The top, left, and right boundaries are set by the spacecraft data storage. The bottom boundary is the actual limb of the planet. The telescope was not stepped. This is a rectified image; that is, to remove gross distortion each scan line was displayed as a different curve depending upon the scanning geometry.

In Table 1 we summarize the Pioneer 11 observations made during the encounter with Jupiter from 18 November until 8 December 1974. The Pioneer 11 trajectory was more highly inclined to Jupiter's equator than that of Pioneer 10. As a result, Pioneer 11 was exposed to lower radiation flux levels for most of the time it was within 10 Jupiter radii (R_J) of the planet. Whereas on Pioneer 10 about a dozen uncommanded changes of instrument state were attributed to radiation, only two or three changes occurred on Pioneer 11.

Our instrument on Pioneer 11 has had a history of slight irregularities in the stepping of the telescope. The telescope will occasionally fail to step, thereby giving redundant rolls of data. During the encounter the problem became substantially worse although the instrument is still functioning. The problem is being analyzed to develop the best possible observing procedures to be used during the coming years of interplanetary cruise and during the encounter with Saturn in December 1979.

The imaging data were displayed in real time by the Pioneer image converter system (PICS) developed by L. R. Baker. This system, located in Pioneer mission control at Ames Research Center, made it possible for the observer team to monitor the instrument operation and the imaging data. The PICS converted the images to color television signals which were fed into a closed-circuit network in the San Francisco area.

As for the finally processed pictures, Figs. 1 and 2 show, respectively, the blue and red images obtained about 6 hours after closest approach (pericenter) which occurred on 3 December 1974 at 6 hours, 2 minutes U.T. At the midtime of these images the spacecraft was 609,000 km from the center of Jupiter, so the imaging field of view, equivalent to one resolution element, subtended a 270-km square on the planet directly beneath the spacecraft. This resolution is slightly better than that of the best Pioneer 10 image. The image is displayed in an orthographic projection onto a plane perpendicular to the line between the spacecraft and the center of the planet at the midtime of the image. The lower left-hand corner of Fig. 2 is overexposed because the instrument gain was set high enough to see detail at dark polar regions. The north pole is off the upper right-hand corner.

The swirling cloud structure near the bottom of Fig. 1 forms the north edge of the North Equatorial Belt. Slanted streaks are seen to its north in the North Tropical Zone. A dark oval structure in this zone is reminiscent of the northern hemisphere red spot in the Pioneer 10 images (*7*); it actually is not the same feature (*11*). Farther to the north, the dark North Temperate Belt shows a smooth southern boundary, but the northern boundary is dark and irregular, drawn out into sharp northeastward-pointing tips. Similar tips are also seen in the two dark belts to its north. At these latitudes ringed and circular features also appear.

Farther to the north the belt and zone structure gives way to less organized detail that is aligned approximately along constant latitudes. Figure 2 shows high-contrast boundaries between very fine light and dark details even at extreme northern latitudes. At these latitudes much more structure is seen in the red than in the blue. As we will show below, this may be because the opacity due to molecular scattering becomes large at high latitudes in blue light.

To illustrate the information content of the photometric data, we will compare the observed intensities and polarizations with those predicted by a simple model consisting of conservative Rayleigh scattering above a Lambert surface. This model was used by Coffeen (*5*) in a preliminary analysis of Pioneer 10 data. While admittedly oversimplified, the model serves to illustrate one type of information—the gas abundance above the clouds—that can be extracted from our data. Accordingly, we next compare the polarization and intensity data along two nearly orthogonal directions in one of our maps with the model. Finally, we comment on the applicability of the model to these data and discuss some of the implications of the data presented.

We chose one of the two directions on the planet to be along the latitude of the South Tropical Zone (STrZ), perhaps the most longitudinally homogeneous region of the planet at the time of flyby, in order to check the consistency of the model over a range of scattering geometries. The free parameters of the model are the optical depth τ of gas above the Lambert surface, and the reflectivity (spherical albedo) A of the Lambert surface. The absolute intensity is arbitrarily multiplied by an intensity calibration constant C before comparison with the data.

Figure 3 shows the observed polarization in the blue channel (0.39 to 0.50 μm) compared to polarizations computed for a range of τ and A. Reasonably good fits are obtained for a variety of A values, at slightly different values of τ as shown in the left half of Fig. 4. The quality of the polarization fit is independent of the value of C.

A successful model must also fit the variation of intensity over the map. Models satisfying the τ,A relation of Fig. 4 are compared with the intensity data in Fig. 5. The fits are good except near the terminator where the models are somewhat too bright and near the bright limb where they do not match the observed decrease in intensity at all. The implications of this decrease are being studied separately (*12*); it may be caused in part by absorption within the Rayleigh layer, which is not included in these models. The relation between C and A for models that fit both intensity and polarization data is given in the right half of Fig. 4. Despite the simplicity of the model, reasonably good agreement between the model and both the intensity and the polarization of blue light is obtained except under conditions of grazing line of sight (spacecraft zenith angle greater than $\sim 70°$) for models obeying the τ,A,C relation of Fig. 4 for the STrZ at a phase angle of 96° (Sun-object-spacecraft angle).

A similar analysis can be carried out on data in red light. The predictions of the simple model do not fit the observed polarization as well. The disagreement is not unexpected, because the molec-

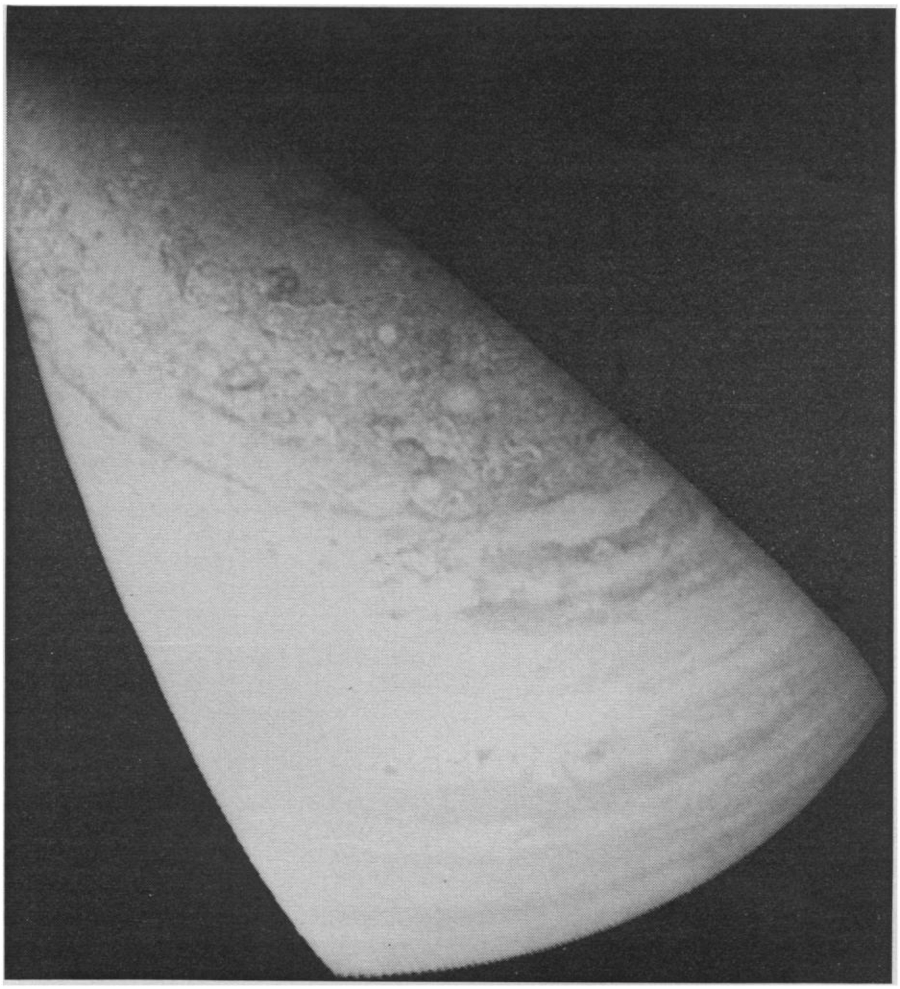

Fig. 2. This complementary image to Fig. 1 in red light (0.595 to 0.70 μm) shows complex detail at high latitudes not seen in blue light. Some dark contrast boundaries especially become visible in red light.

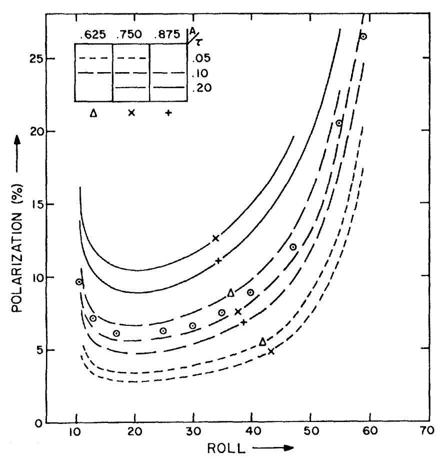

Fig. 3. The observed polarization of blue light scattered by Jupiter's STrZ (circled dots) is plotted against spacecraft roll (numbered from an arbitrary starting roll). Small roll numbers correspond to observations near the limb, and large numbers correspond to observations near the terminator. The observations were made between 2 hours, 43 minutes and 2 hours, 6 minutes before pericenter at a phase angle of $\sim 96°$. The data are compared to seven models having different values of τ and A. Close fits can be found for various values of A by interpolation for τ.

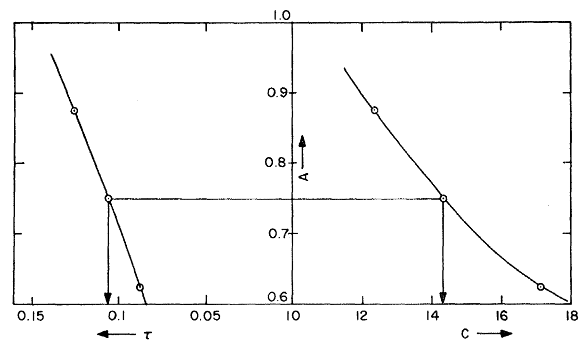

Fig. 4. The relation between τ, A, and C, which the models must obey in order to match the observed variation of polarization and intensity across the STrZ in blue light at a phase angle of 96°. The τ and C values corresponding to $A = 0.75$ are joined by a line.

ular optical depth in red light is only one-fifth as large and residual polarization caused by the aerosols becomes important.

If the absolute calibration of the instrument were now known, the value of C would be determined and we could read specific values for A and τ for the STrZ from Fig. 4. Because the calibration is not yet available, however, we must estimate A from other work before τ can be determined. Correcting Binder and McCarthy's (*13*) value for the geometric albedo ($p \cong 0.47$) of the STrZ at their shortest wavelength (0.59 μm) by the ratio of STrZ reflectivities between 0.59 and 0.44 μm given by Pilcher and McCord (*14*) leads to $p \cong 0.44$ at the effective wavelength of our filter. This corresponds to a value of $A = 0.66$ for the reflectivity of a Lambert surface. However, Binder and McCarthy suspected that their observations were made at a time when the planet was some 10 percent darker than its time average condition. We adopt $A = 0.75$ for the STrZ, giving $\tau = 0.11$ and $C = 14.3$. Although the value for A is somewhat uncertain, Fig. 4 indicates that τ is relatively insensitive to modest changes in A.

Since the model is self-consistent over some range of scattering geometries in the STrZ, it is interesting to apply it to other latitudes. We can use the value of C determined above to find τ and A for the other regions. Figure 6 shows the observed polarization and intensity for a roughly north-south scan obtained before pericenter for the southern hemisphere, and Fig. 7 shows similar data for northern latitudes received after pericenter. The resulting values of τ and A as a function of latitude are given in Table 2. The value of C used for the postpericenter data was adjusted to compensate for a slight decrease in instrument sensibility with time as monitored by an on-board calibration lamp. Table 2 shows a striking increase in the τ value derived from our model with increasing latitude in both hemispheres.

Before reaching any conclusions about Jupiter's atmosphere, however, we briefly discuss the applicability of the

Table 1. Imaging photopolarimeter observing schedule. The time is the number of days (d) or hours (h) before (−) or after (+) Pioneer 11's closest approach to Jupiter at 6 hours, 2 minutes, 21 seconds, Earth Received Time (U.T.). The target is Jupiter (J) or the Galilean satellites, namely Io (I), Europa (II), Ganymede (III), and Callisto (IV). The range is given in Jupiter radii (we used $R_J = 70{,}850$ km), from the planet's center. The phase is the Sun-center of object-spacecraft angle. Mode refers to polarimetry (P) or imaging (I); the number of maps (P) or images (I) obtained during each time interval is given for $\pm$ 24 hours from pericenter.

Time	Target	Range (R_J)	Phase (deg)	Mode
-15^{d} to -7^{d}	J	211–106	40–42	P,I
-15^{d} to -7^{d}	I–IV	211–106	36–49	P
-7^{d} to -1^{d}	J	106–24	42–51	P,I
-7^{d} to -1^{d}	I–IV	106–24	17–80	P
-23^{h}	I	26	63	P
-22^{h}	J	22	52	2I
-21^{h} to -20^{h}	IV	12	80	P,I
-19^{h} to 18.5^{h}	J	20	54	P,I
-16^{h} to -11^{h}	J	18–13	55–60	4P,4I
-10^{h}	III	11	44	I
$+9^{\mathrm{h}}$ to -1^{h}	J	12–2	61–110	8P,4I
$+1^{\mathrm{h}}$ to 10^{h}	J	2–13	92–45	6P,4I
$+11^{\mathrm{h}}$	I	9	97	I
$+12^{\mathrm{h}}$ to 17^{h}	J	14–19	43–40	3P,3I
$+18^{\mathrm{h}}$	III	17	82	P
$+19^{\mathrm{h}}$ to 22^{h}	J	20–23	39–38	2P,2I
$+23^{\mathrm{h}}$	IV	22	105	P
$+1^{\mathrm{d}}$ to 5^{d}	J	24–98	37–32	P.I
$+1^{\mathrm{d}}$ to 5^{d}	I–IV	24–98	67–27	P

Table 2. Latitudinal dependence of optical depth and surface reflectivity (spherical albedo) at 0.44 μm.

Latitude	τ	A
−62.0	0.34	0.52
−60.4	0.36	0.51
−59.8	0.29	0.53
−54.6	0.24	0.49
−49.9	0.22	0.46
−46.3	0.14	0.54
−40.1	0.13	0.49
−35.0	0.12	0.56
−31.0	0.11	0.58
−29.7	0.10	0.60
−24.0	0.10	0.55
−19.5	0.10	0.67
−14.5	0.12	0.70
− 8.9	0.10	0.64
− 2.1	0.09	0.56
+ 1.0	0.10	0.57
+13.2	0.10	0.53
+20.4	0.10	0.68
+29.4	0.12	0.53
+32.8	0.14	0.51
+40.0	0.17	0.52
+45.0	0.19	0.49
+49.9	0.23	0.50
+59.8	0.28	0.50
+65.9	0.28	0.49
+71.3	0.29	0.50
+73.3	0.26	0.48

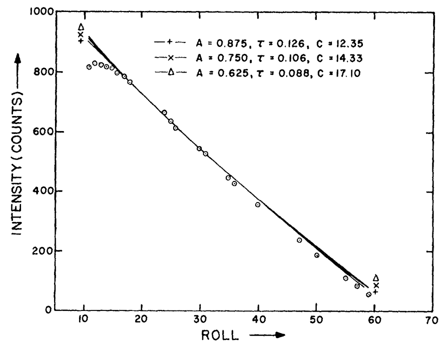

Fig. 5. The circled points are the blue intensity across the STrZ at a phase angle of 96° corresponding to the polarization data of Fig. 3. The solid lines give the intensity predicted by models having three values of A and values of τ required to fit the polarization data. The value of C for each model was determined by scaling the curves to fit the data at roll 30.

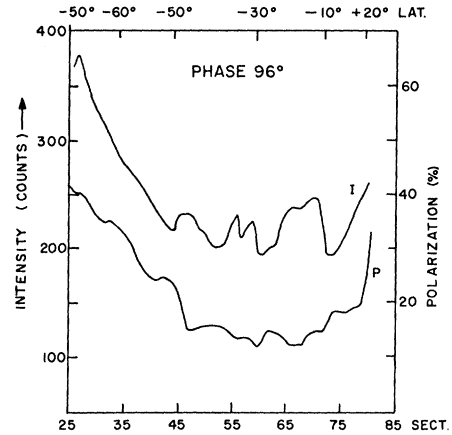

Fig. 6. Intensity and polarization of blue light as a function of sector (representing one field of view) and latitude along a scan in a roughly north-south direction for the southern hemisphere. The data were received 2 hours, 16 minutes before pericenter at a phase angle of ~ 96°.

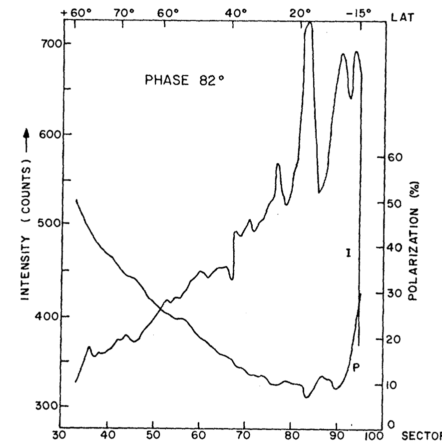

Fig. 7. Intensity and polarization of blue light as a function of sector (representing one field of view) and latitude along a scan in a roughly north-south direction for the northern hemisphere. The data were received 2 hours, 4 minutes after pericenter at a phase angle of ~ 82°.

model used here. The importance of multiple scattering within and between cloud layers has been firmly established for the interpretation of absorption line data for Jupiter with recent analyses (*15–17*) based on a model with a high cloud layer separated by a clear space from a lower, thick cloud. The upper "thin" cloud of the two-layer model is required by absorption line measurements to have a scattering optical depth of the order of 10 for forward-scattering phase laws (*15*). Light that penetrates the upper cloud experiences multiple scattering and should have a polarization upon emergence that is characteristically small compared with that due to Rayleigh single scattering. Therefore, in our analysis of the continuum intensity and polarization data it may be reasonable to neglect the clear space between the cloud layers and treat the clouds as a simple Lambert surface with the polarization arising solely from Rayleigh scattering above the Lambert surface. In this case the τ value derived from our model based on large-phase-angle polarization data should correspond to the optical depth for Rayleigh scattering above the upper cloud of the two-cloud-layer model. On the other hand, if the upper cloud is extremely thin or broken, the correspondence between our model τ and the real atmosphere is not so apparent.

Another shortcoming of the model is the omission of any absorber in the gas above the Lambert surface. Such an absorber may be required to explain the general decrease in albedo of the planet toward shorter wavelength (*16*) and to provide detailed agreement with the large-phase-angle limb darkening. These absorbers could presumably affect the polarization although the agreement of the STrZ polarization with the pure gas model somewhat discounts their importance, at least at this phase angle.

Despite the uncertainties, the model optical depths of Table 2 are of some interest. The optical depth of 0.10 at low latitudes would correspond to Rayleigh scattering from 15 km-amagats of H_2. The addition of He would make a negligible change in τ (since the cross section for Rayleigh scattering by He is much smaller). We note that Trafton and Stone's recent model containing 10 percent He (*18*) has a temperature of ~135°K at the level above which the H_2 abundance is 15 km-amagats. Since in Trafton and Stone's model the saturated vapor pressure of NH_3 equals its partial pressure only a few kilometers below the 135°K level, it is a reasonable location for the top of an NH_3 cloud.

The optical depths of Table 2 increase dramatically at latitudes greater than ~45°. This result cannot be an effect of different scattering geometries since they are not greatly different from those at the lower latitudes. The photons scattered from high-latitude regions have apparently sampled a greater abundance of Rayleigh scatterers (molecules or very small aerosols)—either because the cloud deck actually occurs at a lower elevation, or, should a two-cloud-layer model be applicable in the polar regions, because the upper layer is broken on a scale smaller than one polarization pixel (1700 km), or because the upper layer is thinner. Gehrels *et al.* (*19*) observed stronger wavelength dependence of polarization at the poles of Jupiter than at its limbs near the equator, an effect they attributed to increased Rayleigh scattering at high latitudes. Similarly, in a two-cloud-layer analysis of limb darkening in and out of the CH_4 8900-Å absorption band, Clements (*20*) required the upper cloud layer to be less than 1/5 as thick at +50° latitude than at the STrZ.

We plan to compare our data with more realistic scattering models in the future. We believe that this work will lead to an improved understanding of the cloud structure of Jupiter's atmosphere.

A. L. BAKER, L. R. BAKER
E. BESHORE, C. BLENMAN
N. D. CASTILLO, Y.-P. CHEN
L. R. DOOSE, J. P. ELSTON
J. W. FOUNTAIN, T. GEHRELS
J. H. KENDALL, C. E. KENKNIGHT
R. A. NORDEN, W. SWINDELL
M. G. TOMASKO
University of Arizona, Tucson 85721

D. L. COFFEEN
Goddard Institute for Space Studies, New York 10025

References and Notes

1. T. Gehrels, D. Coffeen, M. Tomasko, L. Doose, W. Swindell, N. Castillo, J. Kendall, A. Clements, J. Hämeen-Anttila, C. KenKnight, C. Blenman, R. Baker, G. Best, L. Baker, *Science* **183**, 318 (1974).
2. S. F. Pellicori, E. E. Russell, L. A. Watts, *Appl. Opt.* **12**, 1246 (1973); a further discussion of spin scan imaging is given by E. E.

Russell and M. G. Tomasko (*Origins Life*, in press).
3. J. L. Weinberg, M. S. Hanner, D. E. Beeson, L. M. DeShields II, B. A. Green, *J. Geophys. Res.* **79**, 3665 (1974).
4. M. S. Hanner, J. L. Weinberg, L. M. DeShields II, B. A. Green, G. N. Toller, *ibid.*, p. 3671.
5. D. L. Coffeen, *ibid.*, p. 3645.
6. M. G. Tomasko, A. E. Clements, N. D. Castillo, *ibid.*, p. 3653.
7. W. Swindell and L. R. Doose, *ibid.*, p. 3634.
8. T. Gehrels, in *Planetary Satellites*, J. A. Burns, Ed. (Cornell Univ. Press, Ithaca, New York, in press).
9. J. W. Fountain, D. L. Coffeen, L. R. Doose, T. Gehrels, W. Swindell, M. G. Tomasko, *Science* **184**, 1279 (1974); T. Gehrels, *J. Geophys. Res.* **79**, 4305 (1974).
10. T. C. Duxbury, *Bull. Am. Astron. Soc.*, in press.
11. B. A. Smith, personal communication.
12. M. G. Tomasko, *Bull. Am. Astron. Soc.*, in press.
- A. B. Binder and D. W. McCarthy, *Astron. J.* **78**, 939 (1973).
- C. B. Pilcher and T. B. McCord, *Astrophys. J.* **165**, 195 (1971).
- R. E. Danielson and M. G. Tomasko, *J. Atmos. Sci.* **26**, 889 (1969).
- L. Axel, *Astrophys. J.* **173**, 451 (1972).
- J. T. Bergstralh, *Icarus* **19**, 390 (1973).
- L. M. Trafton and P. H. Stone, *Astrophys. J.* **188**, 649 (1974).
- T. Gehrels, B. Herman, T. Owen, *Astron. J.* **74**, 190 (1969); a further discussion by T. Gehrels is presented in *Origins Life*, in press.
20. A. E. Clements, thesis, University of Arizona (1974).

21. We thank B. A. Smith for his comments on this paper and M. E. Arthur, G. A. Kew, and J. Golson for their help, especially during the encounter operations. We were able to optimize the performance of our instrument, thanks to the special support we received from the personnel of the Pioneer Project Office, the Bendix Corporation, and NASA's Deep Space Network. Our work is supported by the Pioneer Project Office at NASA Ames Research Center.

14 March 1975

Pioneer 11 Infrared Radiometer Experiment: The Global Heat Balance of Jupiter

Abstract. *Data obtained by the infrared radiometers on the Pioneer 10 and Pioneer 11 spacecraft, over a large range of emission angles, have indicated an effective temperature for Jupiter of 125° ± 3°K. The implied ratio of planetary thermal emission to solar energy absorbed is 1.9 ± 0.2, a value not significantly different from the earth-based estimate of 2.5 ± 0.5.*

Data from the Pioneer 10 and Pioneer 11 infrared radiometers provide a good sample of the infrared emission of Jupiter as a function of latitude and emission angle. Pioneer 10 gave one map in each of two broad spectral channels, each map consisting of an image centered at 11°S on Jupiter (*1*). Pioneer 11 gave two maps in each channel, an inbound map centered at 41°S and a partial outbound map centered at 52°N. About one-half of the outbound viewing period was lost as a result of false commands during passage through the radiation belts. The spatial resolution on Jupiter ranged from 1/30 to 1/200 of the planetary diameter. More than ¾ of the surface area of Jupiter was viewed by the radiometers.

The absolute calibration, with respect to a blackbody, was done in the laboratory before the flight. In-flight calibration, relative to the laboratory value, is provided by a calibrator plate at a known temperature which is moved into the field of view once every 12 seconds (*2*). The zero is set when looking at space, and the response to the calibrator plate is then compared with the response measured in the laboratory. No significant changes occurred during the flight. Both before and after encounter on Pioneer 10 and Pioneer 11 the response in each channel differed from the laboratory value by no more than 3 percent. Our estimates of the uncertainty arising from the calibration procedures range from ±4 to ±8 percent. The latter value will be used throughout this report.

The two spectral channels are centered at wavelengths λ of 20.0 and $\lambda =$ 45.4 μm and have equivalent widths of 11.6 and 22.7 μm, respectively. The measured intensities I_λ are fitted to low-order polynomials in μ and μ_l, where $\mu = \cos\theta$ is the cosine of the emission angle and $\mu_l = \sin l$ is the sine of the latitude. The flux versus latitude $[F_\lambda(\mu_l)]$ and the globally averaged flux $(\bar{F}_\lambda)$ in each channel are then derived from the formulas

$$F_\lambda(\mu_l) = 2\pi \int_0^1 \mu I_\lambda(\mu, \mu_l)\, d\mu$$

and

$$\bar{F}_\lambda = \frac{1}{2}\int_{-1}^{1} \frac{(1 - 2\epsilon\mu_l^2)F_\lambda(\mu_l)\, d\mu_l}{(1 - 2\epsilon/3)}$$

where ε is the oblateness of Jupiter, approximately equal to 0.065 (*3*). Terms of order ε^2 have been neglected.

The values of $F_\lambda(\mu_l)$ and $\bar{F}_\lambda$ depend on the method one employs to average the data, for example, using second-order instead of third-order polynomials, folding the northern and southern hemisphere data together instead of treating them separately, or using Pioneer 10 and Pioneer 11 data combined instead of treating them separately. The spread of values provides an estimate of additional uncertainties that are not included in the ±8 percent associated with the absolute calibration. These additional uncertainties appear to be small. Estimates of $\bar{F}_\lambda$ obtained from Pioneer 10 and Pioneer 11 data treated separately differ from those obtained from the combined data by no more than 3 percent. Different polynomial fits to the combined data give values of $\bar{F}_\lambda$ differing by no more than 1 percent. In addition, the values of $F_\lambda(\mu_l)$ appear to be very nearly independent of latitude, $F_{20}(\mu_l)$ decreasing and $F_{45}(\mu_l)$ increasing from the equator to the pole by about 5 percent, respectively. The values of $\bar{F}_{20}$ and $\bar{F}_{45}$ obtained in this way are 3035 and 5100 erg cm^{-2} sec^{-1}, respectively.

The sum $(\bar{F}_{20} + \bar{F}_{45})$ represents a significant fraction of the average emitted flux $F = \sigma T_e^4$ integrated with respect to wavelength, where σ is the Stefan-Boltzmann constant. The precise value of this fraction depends on the planetary emission in spectral ranges outside the two channels as shown in Table 1. If the planetary emission were to follow a blackbody spectrum, then $F/(F_{20} + F_{45})$ = 1.725. Radiative-convective equilibrium models (*4*), in which the effective temperature T_e and the ratio of He to H_2 are free parameters, give $F/(F_{20} + F_{45}) = 1.723$. Finally, by direct inversion of the intensity data, in which the vertical thermal structure is adjusted so that $I_{20}(\mu)$ and $I_{45}(\mu)$ agree with ob-

Table 1. Estimates of the ratio of the total emitted flux $F = \sigma T_e^4$, integrated with respect to wavelength, to the sum of the fluxes $F_{20} + F_{45}$ observed in the spectral channels of the radiometer.

Description of model	Ratio
Blackbody	
$T_e = 120$°K	1.752
$T_e = 130$°K	1.700
Best fit to $F_{20} + F_{45}$	1.725
Radiative equilbrium (*4*)	
$T_e = 123.8$°K, He/H_2 = 1.0	1.736
$T_e = 131.5$°K, He/H_2 = 1.0	1.673
$T_e = 124.9$°K, He/H_2 = 0.0	1.704
Best fit to $F_{20} + F_{45}$, F_{45}/F_{20}	1.723
Direct thermal inversion (*5*)	
$T_e = 127.9$°K (SEB)	1.694
$T_e = 124.6$°K (STrZ)	1.730
Adopted value (this study)	
$T_e = 125° \pm 3$°K	1.72 ± 0.03